Neuromorphic Silicon Photonics

Alexander N. Tait,* Ellen Zhou, Thomas Ferreira de Lima, Allie X. Wu,
Mitchell A. Nahmias, Bhavin J. Shastri, and Paul R. Prucnal
Princeton University, Princeton, NJ 08544, USA
(Dated: November 9, 2016)

We report first observations of an integrated analog photonic network, in which connections are configured by microring weight banks, as well as the first use of electro-optic modulators as photonic neurons. A mathematical isomorphism between the silicon photonic circuit and a continuous neural model is demonstrated through dynamical bifurcation analysis. Exploiting this isomorphism, existing neural engineering tools can be adapted to silicon photonic information processing systems. A 49-node silicon photonic neural network programmed using a "neural compiler" is simulated and predicted to outperform a conventional approach 1,960-fold in a toy differential system emulation task. Photonic neural networks leveraging silicon photonic platforms could access new regimes of ultrafast information processing for radio, control, and scientific computing.

I. INTRODUCTION

Light forms the global backbone of information transmission yet is rarely used for information transformation, though not for lack of trying [1–3]. Digital optical logic faces fundamental physical challenges [4]. Analog optical co-processors have faced two major economic challenges: optical systems have never achieved competitive manufacturability, nor have they satisfied a sufficiently general processing demand. Incipient changes in the supply and demand for photonics have the potential to spark a resurgence in optical information processing.

A germinating silicon photonic integration industry promises to supply the manufacturing economomies normally reserved for microelectronics. While firmly rooted in demand for datacenter transceivers [5], the industrialization of photonics would impact other application areas [6]. Industrial microfabrication ecosystems propel technology roadmapping [7], library standardization [8, 9], and broadened accessibility [10], all of which could open fundamentally new research directions into large-scale photonic systems. Large-scale beam steerers have been realized [11], and on-chip communication networks have been envisioned [12, 13]; however, opportunities for scalable silicon photonic information processing systems remain largely unexplored.

Concurrently, photonic devices have found analog signal processing niches where electronics can no longer satisfy demands for bandwidth and reconfigurability. This situation is exemplified by radio frequency (RF) processing, in which front-ends have come to be limited by RF electronics, analog-to-digital converters (ADCs), and digital signal processors (DSP) [14, 15]. In response, RF photonics has offered respective solutions for tunable RF filters [16, 17], ADC itself [18], and simple processing tasks that can be moved from DSP into the analog subsystem [19–22]. RF photonic circuits that can be transcribed from fiber to silicon are likely to reap the eco-

nomic benefits of large-*volume* manufacturing. Furthermore, a combination of high-performance analog photonics with an unprecedented opportunity for large-*scale* system integration could lead to fundamentally new concepts, beyond what can be considered in fiber.

Scalable analog processing requires a mathematical framework that provides rules for programming device parameters in order to obtain a desired system behavior. Of models that can bridge this gap, some of the most well-studied and ubiquitous are those of neural networks. Systems that are mathematically isomorphic to neural network models (i.e. neuromorphic systems) can unlock this wealth of existing algorithms [23, 24], proofs [25, 26], and tools [27, 28]. This strategy has experienced recent resurgences in unconventional computing [29–31] and machine learning [32–35] fields, whose reliance on existing theory allows concentration on energy efficient architectures and big data applications, respectively. A contrasting approach, reservoir computing, has recently piqued the interest of the photonics community [36–39]. Reservoir techniques rely on discerning a desired behavior from a large number of un-modeled complex dynamics, taking inspiration from certain brain properties (e.g. analog, distributed), instead of employing a strict isomorphism with a model.

In [40], a silicon-compatible photonic neural networking architecture called "broadcast-and-weight" was proposed. In this architecture, shown in Fig. 1, each node's output is assigned a unique wavelength carrier that is wavelength division multiplexed (WDM) and broadcast to other nodes. Incoming WDM signals are weighted by reconfigurable, continuous-valued filters called microring (MRR) weight banks [41–43] and then summed by total power detection. This electrical weighted sum then modulates the corresponding WDM channel. A nonlinear electro-optic transfer function, such as a laser at threshold or, in this work, a saturated modulator, provides the nonlinearity required for neuron functionality.

Here, we report the first experimental demonstration of an integrated photonic neural network. The network's analog WDM interconnects are reconfigured by silicon MRR weight banks to induce qualitative behavioral tran-

* atait@princeton.edu

sitions (i.e. bifurcations), which serve as observable "fingerprints" of underlying dynamics [44]. The reproduction of neuromorphic bifurcations as a result of reconfiguring MRR weights indicates a mathematical isomorphism between the fabricated sample and a 2-node continuous-time recurrent neural network (CTRNN) model [45]. This result suggests that programming tools for CTRNNs could be applied to larger silicon photonic neural networks.

Silicon photonic CTRNNs could enable new real-time processing capabilities in a range of application domains. Continuous-time neural models have been applied to spectral mining [46], spread spectrum channel estimation [47], and arrayed antenna control [48], and there is insistent demand to implement these functions at wider bandwidths using less power. Additionally, methodologies developed for audio applications, such as noise mitigation [24], could conceivably be employed for RF problems if implemented on ultrafast hardware. A subset of CTRNNs, Hopfield networks [49], have been used extensively in mathematical programming and optimization problems [23]. Photonic hardware accelerators could come to bear on these and other offline problems in scientific computing. As an example of adapting CTRNN design methodology to neuromorphic silicon photonics, we simulate a 49-modulator network programmed using a "neural compiler" [27]. A toy problem of differential equation emulation is used to benchmark the photonic approach against that of a conventional CPU, predicting a hardware acceleration of $1,960\times$.

This work also presents the first investigation of photonic neurons implemented by modulators, as opposed to active laser devices. Interest in laser devices with neuron-like spiking behavior has flourished over the past several years [50, 51], but experimental work has so far focused on isolated neurons [52–54], a linear chain of excitable MRRs [55], and a non-reconfigurable network [56]. This network gap could be explained by the challenges of implementing low-loss, compact, and tunable spectral filters in active III/V platforms required for laser-class neurons. Modulators are compatible with silicon photonic platforms that can also host MRR weight banks. Thus, while laser-class neurons present richer processing opportunities through spiking dynamics, modulator-class neurons could be easier to fabricate, while still possessing the formidable repertoire of CTRNN functions.

II. METHODS

The experimental setup and image of the MRR weight network are shown in Fig. 2. Samples were fabricated on silicon-on-insulator (SOI) wafers at the Washington Nanofabrication Facility through the SiEPIC Ebeam rapid prototyping group [10]. Silicon thickness is 220 nm, and buried oxide (BOX) thickness is 3 µm. 500 nm wide WGs were patterned by Ebeam lithography and fully etched through to the BOX [57]. After a cladding oxide
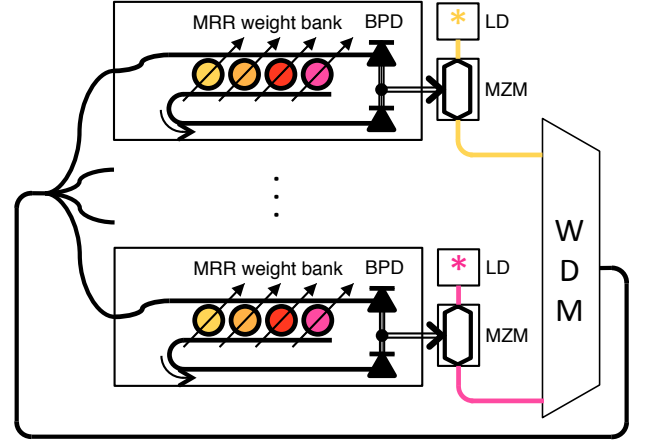

FIG. 1. Concept of a STAR broadcast-and-weight network with modulators used as neurons. MRR: microring resonator, BPD: balanced photodiode, LD: laser diode, MZM: Mach-Zehnder modulator, WDM: wavelength-division multiplexer.

(3 µm) is deposited, Ti/W and Al layers are deposited. Ohmic heating in Ti/W filaments causes thermo-optic resonant wavelength shifts in the MRR weights. The sample is mounted on a temperature stabilized alignment stage and coupled to a 9-fiber array using focusing sub-wavelength grating couplers [58].

The network in a broadcast STAR configuration consists of 2 MRR weight banks each with 4x 10 µm radius MRR weights. Each MRR weight bank is calibrated using the method introduced in Ref. [41, 42]: an offline measurement procedure is performed to identify models of thermo-optic cross-talk and MRR filter edge transmission. During this calibration phase, electrical feedback connections are disabled and the set of wavelength channels carry a set of linearly seperable training signals. After calibration, the user can specify a desired weight matrix, and the control model calculates and applies the corresponding electrical currents.

Weighted network outputs are detected off-chip, and the electrical weighted sums drive fiber Mach-Zehnder modulators (MZMs). Detected signals are low-pass filtered at 10kHz, represented by capacitor symbols in Fig. 2. Low-pass filtering is used to spoil time-delayed dynamics that arise when feedback delay is much greater than the state time-constant [59]. In this setup with on-chip network and off-chip modulator neurons, fiber delayed dynamics would interfere with CTRNN dynamical analysis [60]. MZMs modulating distinct wavelengths λ_1 and λ_2 with neuron output signals $y_1(t)$ and $y_2(t)$, respectively. The MZM electro-optic transfer function serves as the saturating nonlinearity, $y = \sigma'(s)$, associated with the continuous-time neuron. A third wavelength, λ_3, carries an external input signal, $x(t)$, derived from a signal generator. All optical signals (x, y_1, and y_2) are wavelength multiplexed in an arrayed waveguide grating (AWG) and then coupled back into the on-chip broadcast STAR consisting of splitting Y-junctions [61].
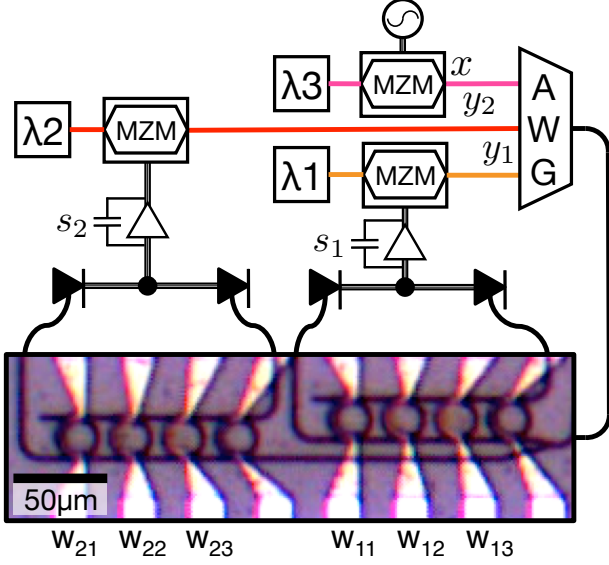
FIG. 2. Experimental setup with two MZM neurons and one external input, wavelength-multiplexed in an arrayed waveguide grating (AWG) and coupled into an on-chip broadcast-and-weight network (pictured). The 2x2 recurrent network is configured by MRR weights, w_{11}, w_{12}, etc. Neuron state is represented by voltages s_1 and s_2 across low-pass filtered transimpedance amplifiers.

III. CUSP BIFURCATION

The CTRNN model is described by a set of ordinary differential equations coupled through a matrix of reconfigurable weights, $\mathbf{W}$.

$$\frac{d\vec{s}(t)}{dt} = \mathbf{W}\vec{y}(t) - \frac{\vec{s}(t)}{\tau} + \vec{w}_{in}x(t) \qquad (1)$$

$$\vec{y}(t) = \sigma'\left[\vec{s}(t)\right] \qquad (2)$$

where $s(t)$ are state variables with timeconstants τ, $y(t)$ are neuron outputs, $\vec{w}_{in}$ are input weights, and $x(t)$ is an external input. σ' is a saturating transfer function associated with each neuron. In this case, the input-output neuron transfer function corresponds to the sinusoidal electro-optic MZM transfer function that accepts the electronic weighted sum and produces a new optical signal. For the sake of analysis, this sinusoidal transfer function is debiased and Taylor expanded to its first nonlinear term.

$$\sigma'(s) \approx \sigma(s) = \alpha s - \kappa s^3 \qquad (3)$$

where $\sigma(s)$ is the debiased approximation, and α and κ are positive coefficients.

Mathematical analysis of dynamical systems begins by examining fixed states (where $\dot{\vec{s}} = 0$) and the effects of parameters on their behavior. Changes in the number or stability of fixed-points, called bifurcations, can be used as observable identifiers of underlying dynamics. The simplest case of (1) is a single node with self feedback:

$$0 = W_F\sigma(s^*) - \frac{s^*}{\tau} + w_{in}x^* \qquad (4)$$

$$= \kappa W_F s^{*3} - \left(\alpha W_F - \tau^{-1}\right)s^* - w_{in}x^* \qquad (5)$$

where s^* and x^* are the steady-state scalar values of the neuron state and input, respectively. The single node with self-feedback weight, W_F, can exhibit several bifurcations between monostable and bistable regimes, which are here derived.

When the input is zero, the steady-state solutions have the form:

$$\kappa W_F s^{*2} = \alpha W_F - \tau^{-1} \qquad (6)$$

$$s^*_{(1)} = 0; \qquad s^*_{(2,3)} = \pm\sqrt{\frac{\alpha}{\kappa}\frac{W_F - W_B}{W_F}} \qquad (7)$$

where $W_B = (\alpha\tau)^{-1}$ is the bifurcation weight, and subscripts index the three solution branches. Below W_B, solution branches (2) and (3) are imaginary and therefore do not physically exist. This expression, plotted on the W_F-y axis of Fig. 3, exhibits the standard form of a pitchfork bifurcation, in which two stable solution branches arise out of one stable branch.

Returning to the general expression, the inputs, x^*, that yield steady-state solutions, s^*, take the form

$$x^* = \frac{\kappa W_F}{w_{in}}\left(s^{*3} - \frac{\alpha}{\kappa}\frac{W_F - W_B}{W_F}s^*\right) \qquad (8)$$

The resulting, familiar S-shaped bistable curve is plotted on the x-y axis of Fig. 3. Three roots of s^* exist when feedback weight is fixed above the pitchfork bifurcation value. The edges of this bistable regime are referred to as saddle-node points because the unstable middle saddle and one of the stable nodes annihilate one another. The saddle-node points s^*_{SN} are found where the derivative of x^* in (8) is zero with respect to s^*.

$$s^*_{SN} = \pm\sqrt{\frac{\alpha}{3\kappa}\frac{W_F - W_B}{W_F}} \qquad (9)$$

Replacing this in (8) arrives at the equation for a cusp

$$x^*_{SN} = \pm\frac{2}{3}\frac{\alpha^{3/2}}{w_{in}\sqrt{3\kappa W_F}}\left(W_F - W_B\right)^{3/2} \qquad (10)$$

which is projected onto the W_F-x axis of Fig. 3. The cusp, a.k.a. fold, bifurcation is more informative than either the pitchfork or saddle-node bifurcations because it is described only in reference to two parameters, while the other bifurcations can occur in systems of one parameter.

A. Results

The theoretical model of a cusp is experimentally observed in the setup described in Sec. II. An external signal generator inputs a 50% duty triangle wave at 3kHz,
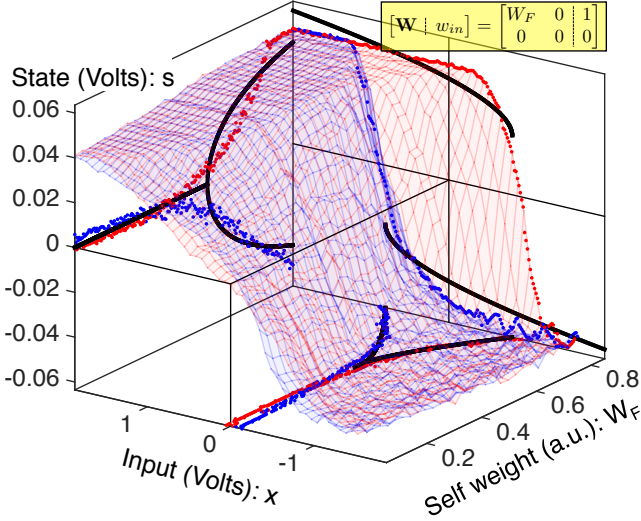
FIG. 3. A cusp bifurcation in a single node with feedback weight, W_F, external input, x, and neurosynaptic state, s. Blue/red grid: increasing/decreasing input. Blue and red data points are taken at slices of the data surfaces; thick black curves are corresponding slices of the theoretical model. Thin lines show planes where slices are taken.

and the feedback weight of node 1 is parameterized as $w_{11} = W_F$. As the feedback weight is swept through 500 points from 0.05–0.85, an oscilloscope captures the input signal, x, and the neurosynaptic signal, s_1. These are plotted against one another in Fig. 3. Since this surface is multi-valued, it is split into lower (blue) and upper (red) branches, corresponding to rising and falling data, respectively. The data are then fit with a theoretical model of the steady-state cusp surface described by (5). The parameters τ, α, and κ are chosen to minimize total root mean squared error between model and data surfaces. Plotted data points are again interpolated from the data surface at the corresponding plane. The best fit model has a cusp at $W_B = 0.54$.

In Fig. 3, the data and fit model surfaces are sliced at $W_F = 0.85$ and plotted in the x-s plane to yield the bistable curve described by (8); plotted data points are taken from the recorded signal at the corresponding weight. The surface is again sliced at $x = 0$ and plotted in the s-W_F plane to yield a pitchfork curve described by (7); plotted data points are interpolated at the corresponding plane. Finally, the surface is sliced at $s = 0$ and plotted on the x-W_F plane to yield the cusp curve described by (10).

The experimental reproduction of pitchfork, bistable, and cusp bifurcations is demonstrative of an isomorphism between the single-node model and the silicon photonic system. An opening of an area between rising and falling data surfaces is characteristic of bistability. More importantly, the transitions between monostable and bistable regimes are mediated by configurations of a MRR weight bank. The transition boundary closely follows a cusp form. Non-idealities in the fit are seen in the pitchfork

and bistable slices, despite their qualitative reproduction of number and growth trends of the stable points. These non-idealities can be attributed to a hard saturation of the electrical transimpedance amplifier when the input voltage and feedback weight are high.

The single-node cusp bifurcation does not constitute a demonstration of a multi-node network. The stable cusp measurements do serve as a control demonstrating the absence of spurious time-delayed oscillations as observed in [60]. In the following section, we study an oscillatory bifurcation that can only occur in multi-node dynamical systems.

IV. HOPF BIFURCATION

Dynamical systems are capable of oscillating if there exists a closed orbit (a.k.a. limit cycle) in the state space, which must therefore exceed one dimension. The Andronov-Hopf (Hopf) bifurcation occurs when a stable fixed-point becomes unstable while giving rise to a stable limit cycle. Hopf bifurcations are further characterized by oscillations that approach zero amplitude and nonzero frequency near the bifurcation point [62].

A Hopf bifurcation can arise in a two node neural network described by (1) under proper conditions. We fix the off-diagonal weights asymmetrically such that $-w_{12} = w_{21} = 1$ and parameterize the diagonals such that $w_{11} = w_{22} = W_F$. As before, W_F is used to indicate self feedback weight. Under this formulation, there is always one and only one steady-state at $\vec{s} = 0$. To examine its stability, we linearize the system around this point to yield the Jacobian matrix whose eigenvalues indicate fixed-point stability.

$$\mathbf{J} = \frac{d}{ds}\left(\frac{ds}{dt}\right) = \alpha \begin{bmatrix} W_F - (\alpha\tau)^{-1} & -1 \\ 1 & W_F - (\alpha\tau)^{-1} \end{bmatrix} (11)$$

which has eigenvalues

$$\lambda = W_F - (\alpha\tau)^{-1} \pm i \qquad (12)$$

The imaginary part of the eigenvalue pair is indicative of oscillating behavior. The real part of the eigenvalue switches sign at the bifurcation weight $W_B = (\alpha\tau)^{-1}$. In this case, when the only fixed-point solution becomes unstable, a stable limit cycle arises instead of new stable states. Near threshold, we can assume a circular form of the limit cycle in order to model its expected amplitude, A, and frequency, ω.

$$s_1(t) = A\sin(\omega t); \quad s_2(t) = A\cos(\omega t) \qquad (13)$$

At points where ωt is a multiple of 2π, the time-derivative of s_2 is zero. Examining the $\dot{s}_2$ equation from (1),

$$\left.\frac{ds_2}{dt}\right|_{\omega t = 2\pi m} = 0 = \sigma(0) + W_F\sigma(A) - \tau^{-1}A \qquad (14)$$

$$= \alpha(W_F - W_B)A - W_F\kappa A^3 \qquad (15)$$

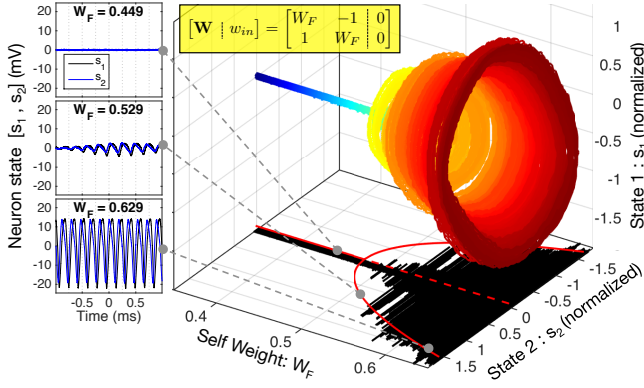$$A = \sqrt{\frac{\alpha}{\kappa}\frac{W_F - W_B}{W_F}} \qquad (16)$$

FIG. 4. A Hopf bifurcation between stable and oscillating states. Off-diagonal weights are asymmetric and diagonal self weights are swept in concert. Color represents feedback weight parameter, W_F. Black shadow: average experimental amplitudes; solid red curve: corresponding fit model; dotted red line: unstable solution. Insets show time traces below, near, and above the bifurcation.

where m is an integer. The amplitude follows a form similar to that of the pitchfork bifurcation in (7). The equation for $\dot{s}_1$ at this same point can be used to find the angular frequency.

$$\left. \frac{ds_1}{dt} \right|_{\omega t = 2\pi m} = -A\omega = W_F \sigma(0) - \sigma(A) \quad (17)$$

$$\omega = \alpha - \kappa A^2 \quad (18)$$

$$= \frac{\tau^{-1}}{W_F} \quad (19)$$

The expected limit cycle frequency is therefore finite at the Hopf point and inversely proportional above.

A. Results

We experimentally reproduce the model predictions of oscillation, amplitude, and frequency by parameterizing the network's MRR weights as described above and varying them together. The insets of Fig. 4 show the time traces for below, near, and above the oscillation threshold. Near threshold, transient oscillations with non-constant envelope can be triggered by noise. Above threshold, oscillation occurs in the range of 1-10kHz, as limited by electronic low-pass filters and feedback delay.

Fig. 4 shows the result of a fine sweep of self-feedback weights in the 2-node network, exhibiting the paraboloid shape of a Hopf bifurcation. W_F is swept over 300 points from 0.35 to 0.65 while off-diagonal weights are fixed and asymmetric. The voltage of neuron 1 is plotted against that of neuron 2 with color corresponding to W_F parameter. The peak oscillation amplitude for each weight is then projected onto the $W_F - y_2$ plane in black, and these amplitudes are fit using the model from (16) (red). Bifurcation occurs at $W_B = .48$ in the fit model.

Fig. 5 plots the oscillation frequency above the Hopf point. The frequency is determined by detecting positive zero-crossings in $s_1(t)$ and calculating based on time differences. Data are discarded for $W_B < W_F < 0.53$ because the oscillations are erratic in the sensitive transition region. Frequency data are then fit with the model of (19). The frequency axis is scaled so that 1.0 corresponds to the model frequency at region boundary, which is 4.81 kHz. The Hopf bifurcation only occurs in systems of more than one dimension, thus confirming the observation of a small integrated photonic neural network.

Significantly above the bifurcation point, experimental oscillation amplitude and frequency closely match model predictions. Discrepancies between model and observations in Figs. 4 and 5 are apparent in the sensitive transition range of $W_B < W_F < 0.53$. Near the bifurcation point, the time required to converge to a stable limit cycle is significantly greater than those further above the bifurcation. If the oscillation does not have time to stabilize within the recording window, its equilibrium amplidude is underestimated. Another potential source of discrepancy is noise, which was not included in the model. Limit cycles with amplitudes comparable to noise amplitude can be destabilized by their proximity to the unstable fixed point at zero. This effect could explain the middle inset of Fig. 4, in which a small oscillation grows and then shrinks.

Finally, part of this discrepancy can be explained by weight inaccuracy. The two MRR weight banks were calibrated independently using the method in Ref. [42]; however, thermal cross-talk between different banks was not accounted for. As seen in Fig. 2, the physical distance between w_{12} (nominally –1) and w_{22} (nominally W_F) is approximately 100 μm. While inter-bank crosstalk is not a major effect, w_{12} is very sensitive because weight –1 corresponds to on-resonance, and the dynamics are especially sensitive to the weight values near the bifurcation point. This source of weight inaccuracy was not present in the cusp bifurcation of Sec. III because only one weight bank was dynamically changing.

V. SYSTEM DESIGN EXAMPLE

The primary result of this article is the demonstration of a dynamical isomorphism between a silicon photonic system and the CTRNN model of (1). This result means that larger, faster silicon photonic systems of an analogous form could utilize existing tools for neural network models. In this section, we present an example application design flow of a photonic network of MZM-type neurons guided by the Neural Engineering Framework (NEF) [63]. We simulate a network of 49 MZM neurons solving a user-specified ordinary differential equation (ODE) and then benchmark its performance against a conventional computer solving the same ODE.

Systems of ODEs are ubiquitous in computational problems [64–66], a fact that has motivated the develop-
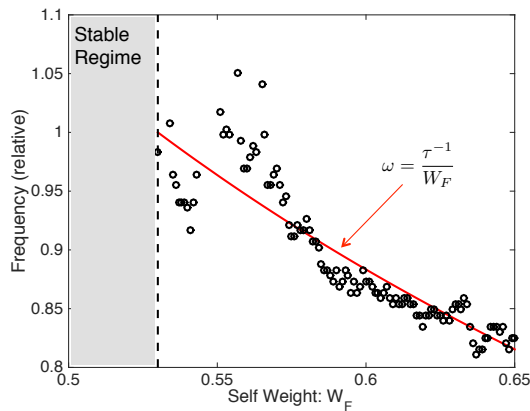
FIG. 5. Frequency of oscillation above the Hopf bifurcation. The observed data (black points) are compared to the expected trend of (19) (red curve). Frequencies are normalized to the threshold frequency of 4.81 kHz.

ment of specialized hardware [67]. Hardware emulators, as opposed to software simulators, are typically analog systems that can be configured to exhibit the same dynamics as the variables in the ODE of interest. For some problems, emulators can reap significant speed or energy improvements compared to a conventional digital computer performing the corresponding simulation [68]. Beyond performance, a central consideration of emulators is the breadth of problems that can be emulated. The large configurability offered by neural network weights is an advantage in this regard, but also presents a challenge in determining how to program the weights.

The NEF provides a procedure to take in an arbitrary ODE and return a weight matrix that will result in its emulation by a CTRNN. An advantage of the NEF over other neural frameworks (e.g. layered perceptrons) is that it does not rely on adaptation, but instead guarantees a deterministic solution for arbitrary problems of certain classes, including ODE emulation. These characteristics shared by digital compilers have motivated a designation of "neural compiler." While originally developed to evaluate theories of cognition, the NEF has been appropriated to solve engineering problems [69] and has been used to program electronic neuromorphic hardware [70].

We use a benchmark task of ODE emulation to compare the performance of a photonic CTRNN against that of a conventional CPU. As opposed to implementation-level metrics, such as clock speed or transistor leakage current, benchmarks are task-level indicators well suited for comparing disparate technologies. A variety of neuromorphic electronic architectures are benchmarked in [71], and benchmark tasks for embedded systems are proposed in [72]. In this case, fundamental implementation differences between digital computers and neural networks limit the meaningfulness of device-level metrics. We take advantage of the NEF's compiler interface to establish a

benchmark based on solving the classic Lorenz attractor:

$$
\begin{aligned}
\dot{x}_0 &= \sigma(x_1 - x_0) \\
\dot{x}_1 &= -x_0 x_2 - x_1 \\
\dot{x}_2 &= x_0 x_1 - \beta(x_2 + \rho) - \rho
\end{aligned}
\tag{20}
$$

With default parameters: $(\sigma, \beta, \rho) = (10, 8/3, 28)$, the solutions of the system are chaotic.

A. Photonic CTRNN Emulator

The NEF approximates functions $\vec{f}(\vec{x})$ using a linear combination of given neural tuning curves across the domain of values of $\vec{x}$ considered. Simulation variables, $\vec{x}$, are represented by linear combinations of real network states, $\vec{s}$. Each neuron in a population has the same σ tuning curve, differing in gain g, encoder vector α and offset b, such that $y_i = \sigma(g_i \vec{\alpha}_i \cdot \vec{s} + b_i)$. Introducing recurrent connections in the population provides effective dynamical system of the form $\dot{\vec{x}} = \vec{f}(\vec{x})$. We specify the tuning curve as the sinusoidal electro-optic transfer characteristic of a MZM, and we specify the system of interest according to the three variable Lorenz system of (20). The NEF then provides the recurrent weight matrix, $\mathbf{W}$, that results in effective emulation.

Modifications to the standard NEF procedure were made to exploit the relation of the MZM transfer function to the Fourier basis, thereby reducing the number of neurons needed. Instead of drawing encoders randomly, they were selected as the vertices of a unit-cube $\alpha = [\pm 1, \pm 1, \pm 1]$. Gains were chosen to correspond to the first three Fourier frequencies of the domain: $g \in \{s_\pi/2, s_\pi, 3s_\pi/2\}$, where s_π is the MZM function half-period. Offsets were chosen to be $b \in \{0, s_\pi/2\}$. An extra neuron with constant output is added to account for the zero-frequency of the Fourier decomposition. The total number of neurons is therefore $\#\alpha \cdot \#g \cdot \#b + 1 = 8 \cdot 3 \cdot 2 + 1 = 49$.

The operational speed of the system is determined by the synaptic timeconstant, τ, that is equivalent to the silicon MZM timeconstant. Silicon MZMs with 40 GHz bandwidths are now common [73, 74]; however, feedback latency is the limiting factor as it must be less than the synaptic timeconstants. Supposing a network with the geometry of Fig. 1, the longest feedback path is via the drop port of the last (pink) MRR weight of the first (yellow) neuron's bank. If the number of neurons is $N=49$, and the MRR pitch is $D \approx 20\,\mu\text{m}$, then the maximum feedback length is $L = ND(1 + 2 + 3)$, where summands respectively correspond to the first pass through the bank, the drop waveguide path, and the feedback waveguide path. In this example, the feedback latency nL/c is therefore 69 ps, meaning the modulator driver circuitry must be low-pass filtered. In the simulation of the hardware neural network, we choose $\tau = 100\text{ps}$.
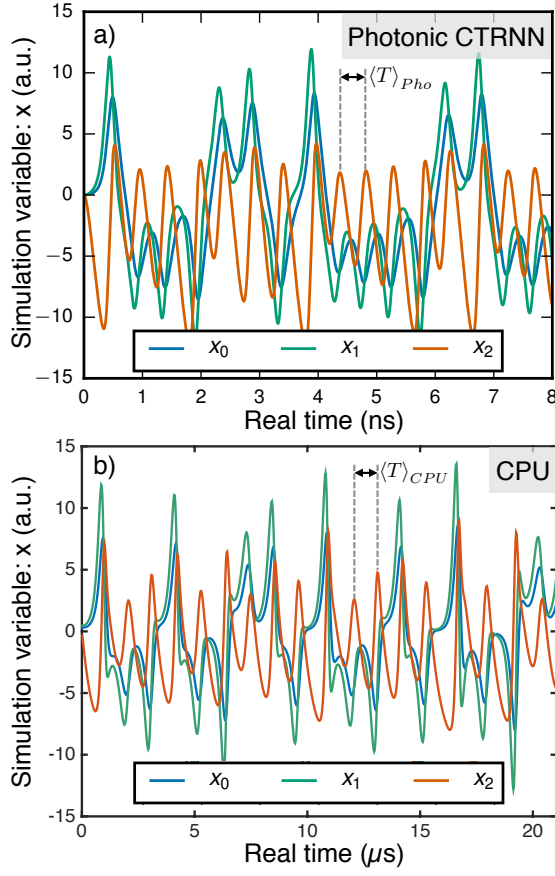
FIG. 6. a) Simulation of a continuous-time silicon photonic neural network emulator, programmed using NEF. b) Conventional discrete-time ODE simulation. Time windows cover equal intervals of emulation time, as measured by x_2 crossing intervals, $\langle T \rangle$. Time axes are scaled by τ and Δt, respectively, showing a real time acceleration of 1,960×.

B. CPU Simulator

Conventional processors use a discrete-time approximation to simulate continuous ODEs, the simplest of which is Euler continuation:

$$\vec{x}[(n+1)\Delta t] = \vec{x}[n\Delta t] + \Delta t \vec{f}(\vec{x}[n\Delta t]) \qquad (21)$$

where Δt is the time step interval, which is related to both simulation time and physical real time.

To estimate the physical time value of Δt, we develop and validate a simple CPU model. For each time step, the CPU must compute $\vec{f}(\vec{x}[n\Delta t])$ as defined in (20), resulting in 9 floating-point operations (FLOPs), and 12 cache reads of the operands. The Euler update in (21) constitutes one multiply, one addition, and one read/write for each state variable, resulting in 6 FLOPs and 6 cache accesses. With a FLOP latency of 1 clock cycle, Level 1 (L1) cache latency of 4 cycles [75], and 2.6GHz clock, this model predicts a time step of Δt =33 ns. This model is empirically validated using an Intel Core i5-4288U [75]. The machine-optimized program randomly

initializes and loops through 10^6 Euler steps of the Lorenz system, over 100 trials. CPU time was measured to be $\Delta t = 24.5 \pm 1.5$ns. We note that CPU architectures can vary significantly, including in ways that could accelerate performance on this specific task (e.g. by keeping operands in registers), but mean for this model to serve as a quantifiable baseline.

C. Benchmarking

The discrete-time simulation and continuous-time emulation are linked to physical real time by the varibles Δt and τ, but must be benchmarked using a common emulation/simulation time basis. An emulation/simulation time basis can be established based on the well-behaved x_2 variable, whose zero-crossing interval is heretofore referred to as $\langle T \rangle$. Simulations of the photonic CTRNN exhibited $\langle T \rangle_{Pho} = 5.0\tau$. In the discrete-time case, the simulation time step is limited by numerical instability stemming from discretization. We performed a series of 100 trials over 100 values of $\Delta t / \langle T \rangle_{CPU}$, finding that 100% stability occurred for $\Delta t \leq 0.025 \langle T \rangle_{CPU}$. Mapping the emulation time reference to physical time results in $\langle T \rangle_{Pho} = 0.50$ ns, and $\langle T \rangle_{CPU} = 980$ ns. The effective hardware acceleration factor of the photonic neural network is therefore estimated to be *1,960 ×* in this task.

More significant than an identified performance improvement is the procedure for compiling arbitrary dynamical emulation tasks into a neuromorphic silicon photonic system. Because of the isomorphism demonstrated in Sec. III- IV, analogous procedures could be developed using other CTRNN tools. This excercise suffers from the limited relevance of toy problems in addition to neglecting optimizations possible in digital technologies (e.g. field-programmable gate arrays). Nevertheless, the general approach of benchmarking, enabled by task-level neural network programming, could be refined extensively to assess the potentials of neuromorphic photonics in specific application domains.

VI. CONCLUSION

We have demonstrated a reconfigurable analog neural network in a silicon photonic integrated circuit using modulators as neuron elements. Network-mediated cusp and Hopf bifurcations were observed as a first proof-of-concept of an integrated broadcast-and-weight system [40]. Neural network abstractions are powerful tools for bridging the gap between physical dynamics and useful application, and silicon photonic manufacturing introduces opportunities for large-scale photonic systems. Simulations of a 49 modulator neuron network performing an emulation task estimated a 1,960× speedup over a verified CPU benchmark. At increased scale, silicon photonic neural networks could be applied to unaddressed computational areas requiring ultrafast, reconfigurable,

and efficient hardware processors. Furthermore, silicon photonic neural networks could represent first forays into a broader class of silicon photonic systems for scalable information processing.

[1] O. A. Reimann and W. F. Kosonocky, "Progress in optical computer research," IEEE Spectrum **2**, 181–195 (1965).

[2] F. B. McCormick, T. J. Cloonan, F. A. P. Tooley, A. L. Lentine, J. M. Sasian, J. L. Brubaker, R. L. Morrison, S. L. Walker, R. J. Crisci, R. A. Novotny, S. J. Hinterlong, H. S. Hinton, and E. Kerbis, "Six-stage digital free-space optical switching network using symmetric self-electro-optic-effect devices," Appl. Opt. **32**, 5153–5171 (1993).

[3] S. Jutamulia and F. Yu, "Overview of hybrid optical neural networks," Optics & Laser Technology **28**, 59 – 72 (1996).

[4] R. W. Keyes, "Optical logic-in the light of computer technology," Optica Acta: International Journal of Optics **32**, 525–535 (1985).

[5] Y. Vlasov, "Silicon CMOS-integrated nano-photonics for computer and data communications beyond 100G," IEEE Commun. Mag. **50**, s67–s72 (2012).

[6] M. Hochberg, N. C. Harris, R. Ding, Y. Zhang, A. Novack, Z. Xuan, and T. Baehr-Jones, "Silicon photonics: The next fabless semiconductor industry," IEEE Solid-State Circuits Magazine **5**, 48–58 (2013).

[7] D. Thomson, A. Zilkie, J. E. Bowers, T. Komljenovic, G. T. Reed, L. Vivien, D. Marris-Morini, E. Cassan, L. Virot, J.-M. Fédéli, J.-M. Hartmann, J. H. Schmid, D.-X. Xu, F. Boeuf, P. O'Brien, G. Z. Mashanovich, and M. Nedeljkovic, "Roadmap on silicon photonics," Journal of Optics **18**, 073003 (2016).

[8] A.-J. Lim, J. Song, Q. Fang, C. Li, X. Tu, N. Duan, K. K. Chen, R.-C. Tern, and T.-Y. Liow, "Review of silicon photonics foundry efforts," IEEE J. Sel. Top. Quantum Electron. **20**, 405–416 (2014).

[9] J. S. Orcutt, B. Moss, C. Sun, J. Leu, M. Georgas, J. Shainline, E. Zgraggen, H. Li, J. Sun, M. Weaver, S. Urošević, M. Popović, R. J. Ram, and V. Stojanović, "Open foundry platform for high-performance electronic-photonic integration," Opt. Express **20**, 12222–12232 (2012).

[10] L. Chrostowski and M. Hochberg, *Silicon Photonics Design: From Devices to Systems* (Cambridge University Press, 2015).

[11] J. Sun, E. Timurdogan, A. Yaacobi, Z. Su, E. Hosseini, D. Cole, and M. Watts, "Large-scale silicon photonic circuits for optical phased arrays," Selected Topics in Quantum Electronics, IEEE Journal of **20**, 264–278 (2014).

[12] R. G. Beausoleil, "Large-scale integrated photonics for high-performance interconnects," J. Emerg. Technol. Comput. Syst. **7**, 6:1–6:54 (2011).

[13] S. Le Beux, J. Trajkovic, I. O'Connor, G. Nicolescu, G. Bois, and P. Paulin, "Optical ring network-on-chip (ORNoC): Architecture and design methodology," in "Design, Automation Test in Europe Conference Exhibition (DATE), 2011," (2011), pp. 1–6.

[14] J. Capmany, J. Mora, I. Gasulla, J. Sancho, J. Lloret, and S. Sales, "Microwave photonic signal processing," Journal of Lightwave Technology **31**, 571–586 (2013).

[15] A. Farsaei, Y. Wang, R. Molavi, H. Jayatilleka, M. Caverley, M. Beikahmadi, A. H. M. Shirazi, N. Jaeger, L. Chrostowski, and S. Mirabbasi, "A review of wireless-photonic systems: Design methodologies and topologies, constraints, challenges, and innovations in electronics and photonics," Optics Communications pp. – (2016).

[16] N.-N. Feng, P. Dong, D. Feng, W. Qian, H. Liang, D. C. Lee, J. B. Luff, A. Agarwal, T. Banwell, R. Menendez, P. Toliver, T. K. Woodward, and M. Asghari, "Thermally-efficient reconfigurable narrowband rf-photonic filter," Opt. Express **18**, 24648–24653 (2010).

[17] L. Zhuang, C. G. H. Roeloffzen, M. Hoekman, K.-J. Boller, and A. J. Lowery, "Programmable photonic signal processor chip for radiofrequency applications," Optica **2**, 854–859 (2015).

[18] G. C. Valley, "Photonic analog-to-digital converters," Opt. Express **15**, 1955–1982 (2007).

[19] M. H. Khan, H. Shen, Y. Xuan, L. Zhao, S. Xiao, D. E. Leaird, A. M. Weiner, and M. Qi, "Ultrabroad-bandwidth arbitrary radiofrequency waveform generation with a silicon photonic chip-based spectral shaper," Nature: Photonics **4**, 117–122 (2010).

[20] J. Chang, J. Meister, and P. R. Prucnal, "Implementing a novel highly scalable adaptive photonic beamformer using "blind" guided accelerated random search," Journal of Lightwave Technology **32**, 3623–3629 (2014).

[21] T. Ferreira de Lima, A. N. Tait, M. A. Nahmias, B. J. Shastri, and P. R. Prucnal, "Scalable wideband principal component analysis via microwave photonics," IEEE Photonics Journal **8**, 1–9 (2016).

[22] G.-k. Chang and L. Cheng, "The benefits of convergence," Philosophical Transactions of the Royal Society A: Mathematical, Physical and Engineering Sciences **374**, 20140442 (2016).

[23] U.-P. Wen, K.-M. Lan, and H.-S. Shih, "A review of hopfield neural networks for solving mathematical programming problems," European Journal of Operational Research **198**, 675 – 687 (2009).

[24] T. Lee and F. Theunissen, "A single microphone noise reduction algorithm based on the detection and reconstruction of spectro-temporal features," Proceedings of the Royal Society of London A: Mathematical, Physical and Engineering Sciences **471** (2015).

[25] D. J. C. MacKay, "A practical Baysian framework for backpropagation networks," Neural Computation **4**, 448–472 (1992).

[26] K. Hornik, M. Stinchcombe, and H. White, "Multilayer feedforward networks are universal approximators," Neural Networks **2**, 359–366 (1989).

[27] C. Eliasmith and C. H. Anderson, *Neural engineering: Computation, representation, and dynamics in neurobiological systems* (MIT Press, 2004).

[28] F. Donnarumma, R. Prevete, A. de Giorgio, G. Montone, and G. Pezzulo, "Learning programs is better than learning dynamics: A programmable neural network hierarchical architecture in a multi-task scenario," Adaptive Behavior **24**, 27–51 (2016).

[29] P. A. Merolla, J. V. Arthur, R. Alvarez-Icaza, A. S. Cassidy, J. Sawada, F. Akopyan, B. L. Jackson, N. Imam, C. Guo, Y. Nakamura, B. Brezzo, I. Vo, S. K. Esser, R. Appuswamy, B. Taba, A. Amir, M. D. Flickner, W. P. Risk, R. Manohar, and D. S. Modha, "A million spiking-neuron integrated circuit with a scalable communication network and interface," Science **345**, 668–673 (2014).

[30] F. Akopyan, J. Sawada, A. Cassidy, R. Alvarez-Icaza, J. Arthur, P. Merolla, N. Imam, Y. Nakamura, P. Datta, G.-J. Nam, B. Taba, M. Beakes, B. Brezzo, J. Kuang, R. Manohar, W. Risk, B. Jackson, and D. Modha, "Truenorth: Design and tool flow of a 65 mw 1 million neuron programmable neurosynaptic chip," IEEE Trans. Comput. Aided Des. Integr. Circuits Syst. **34**, 1537–1557 (2015).

[31] G. Indiveri and S.-C. Liu, "Memory and information processing in neuromorphic systems," arXiv:1506.03264 (2015).

[32] Y. Lecun, L. Bottou, Y. Bengio, and P. Haffner, "Gradient-based learning applied to document recognition," Proceedings of the IEEE **86**, 2278–2324 (1998).

[33] G. E. Hinton, S. Osindero, and Y.-W. Teh, "A fast learning algorithm for deep belief nets," Neural Computation **18**, 1527–1554 (2006).

[34] Y. LeCun, Y. Bengio, and G. Hinton, "Deep learning," Nature **521**, 436–444 (2015).

[35] D. Silver, A. Huang, C. J. Maddison, A. Guez, L. Sifre, G. van den Driessche, J. Schrittwieser, I. Antonoglou, V. Panneershelvam, M. Lanctot, S. Dieleman, D. Grewe, J. Nham, N. Kalchbrenner, I. Sutskever, T. Lillicrap, M. Leach, K. Kavukcuoglu, T. Graepel, and D. Hassabis, "Mastering the game of go with deep neural networks and tree search," Nature **529**, 484–489 (2016).

[36] D. Brunner, M. C. Soriano, C. R. Mirasso, and I. Fischer, "Parallel photonic information processing at gigabyte per second data rates using transient states," Nat Commun **4**, 1364 (2013).

[37] K. Vandoorne, P. Mechet, T. Van Vaerenbergh, M. Fiers, G. Morthier, D. Verstraeten, B. Schrauwen, J. Dambre, and P. Bienstman, "Experimental demonstration of reservoir computing on a silicon photonics chip," Nat Commun **5** (2014).

[38] M. C. Soriano, D. Brunner, M. Escalona-Morán, C. R. Mirasso, and I. Fischer, "Minimal approach to neuro-inspired information processing," Frontiers in Computational Neuroscience **9**, 68 (2015).

[39] F. Duport, A. Smerieri, A. Akrout, M. Haelterman, and S. Massar, "Fully analogue photonic reservoir computer," Scientific Reports **6**, 22381 EP – (2016).

[40] A. N. Tait, M. A. Nahmias, B. J. Shastri, and P. R. Prucnal, "Broadcast and weight: An integrated network for scalable photonic spike processing," J. Lightwave Technol. **32**, 3427–3439 (2014).

[41] A. Tait, T. Ferreira de Lima, M. Nahmias, B. Shastri, and P. Prucnal, "Continuous calibration of microring weights for analog optical networks," Photonics Technol. Lett. **28**, 887–890 (2016).

[42] A. N. Tait, T. Ferreira de Lima, M. A. Nahmias, B. J. Shastri, and P. R. Prucnal, "Multi-channel control for microring weight banks," Opt. Express **24**, 8895–8906 (2016).

[43] A. N. Tait, A. X. Wu, T. Ferreira de Lima, E. Zhou, B. J. Shastri, M. A. Nahmias, and P. R. Prucnal, "Microring weight banks," IEEE Journal of Selected Topics in Quantum Electronics **PP**, 1–1 (2016).

[44] A. Tait, A. Wu, E. Zhou, T. Ferreira de Lima, M. Nahmias, B. Shastri, and P. Prucnal, "Demonstration of a silicon photonic neural network," in "Summer Topicals Meeting Series (SUM), 2016," (IEEE, 2016).

[45] R. D. Beer, "On the dynamics of small continuous-time recurrent neural networks," Adaptive Behavior **3**, 469–509 (1995).

[46] V. K. Tumuluru, P. Wang, and D. Niyato, "A neural network based spectrum prediction scheme for cognitive radio," in "Communications (ICC), 2010 IEEE International Conference on," (2010), pp. 1–5.

[47] U. Mitra and H. V. Poor, "Neural network techniques for adaptive multiuser demodulation," IEEE Journal on Selected Areas in Communications **12**, 1460–1470 (1994).

[48] K.-L. Du, A. Lai, K. Cheng, and M. Swamy, "Neural methods for antenna array signal processing: a review," Signal Processing **82**, 547 – 561 (2002).

[49] J. J. Hopfield and D. W. Tank, ""neural" computation of decisions in optimization problems," Biological Cybernetics **52**, 141–152 (1985).

[50] M. A. Nahmias, B. J. Shastri, A. N. Tait, and P. R. Prucnal, "A leaky integrate-and-fire laser neuron for ultrafast cognitive computing," IEEE J. Sel. Top. Quantum Electron. **19**, 1–12 (2013).

[51] P. R. Prucnal, B. J. Shastri, T. Ferreira de Lima, M. A. Nahmias, and A. N. Tait, "Recent progress in semiconductor excitable lasers for photonic spike processing," Adv. Opt. Photon. **8**, 228–299 (2016).

[52] F. Selmi, R. Braive, G. Beaudoin, I. Sagnes, R. Kuszelewicz, and S. Barbay, "Relative refractory period in an excitable semiconductor laser," Phys. Rev. Lett. **112**, 183902 (2014).

[53] B. Romeira, R. Avó, J. L. Figueiredo, S. Barland, and J. Javaloyes, "Regenerative memory in time-delayed neuromorphic photonic resonators," Scientific Reports **6**, 19510 EP – (2016).

[54] M. A. Nahmias, A. N. Tait, L. Tolias, M. P. Chang, T. Ferreira de Lima, B. J. Shastri, and P. R. Prucnal, "An integrated analog O/E/O link for multi-channel laser neurons," Applied Physics Letters **108**, 151106 (2016).

[55] T. V. Vaerenbergh, M. Fiers, P. Mechet, T. Spuesens, R. Kumar, G. Morthier, B. Schrauwen, J. Dambre, and P. Bienstman, "Cascadable excitability in microrings," Opt. Express **20**, 20292–20308 (2012).

[56] B. J. Shastri, M. A. Nahmias, A. N. Tait, A. W. Rodriguez, B. Wu, and P. R. Prucnal, "Spike processing with a graphene excitable laser," Sci. Rep. **5**, 19126 (2015).

[57] R. J. Bojko, J. Li, L. He, T. Baehr-Jones, M. Hochberg, and Y. Aida, "Electron beam lithography writing strategies for low loss, high confinement silicon optical waveguides," J. Vac. Sci. Technol., B **29** (2011).

[58] Y. Wang, X. Wang, J. Flueckiger, H. Yun, W. Shi, R. Bojko, N. A. Jaeger, and L. Chrostowski, "Focusing subwavelength grating couplers with low back reflections for rapid prototyping of silicon photonic circuits," Opt. Express **22**, 20652–20662 (2014).

[59] B. Romeira, F. Kong, W. Li, J. M. Figueiredo, J. Javaloyes, and J. Yao, "Broadband chaotic signals and breather oscillations in an optoelectronic oscillator incorporating a microwave photonic filter," Lightwave Technology, Journal of **32**, 3933–3942 (2014).

[60] E. Zhou, A. Tait, A. Wu, T. Ferreira de Lima, M. Nahmias, B. Shastri, and P. Prucnal, "Silicon photonic weight bank control of integrated analog network dynamics," in "Optical Interconnects Conference, 2016 IEEE," (IEEE, 2016), p. TuP9.

[61] Y. Zhang, S. Yang, A. E.-J. Lim, G.-Q. Lo, C. Galland, T. Baehr-Jones, and M. Hochberg, "A compact and low loss y-junction for submicron silicon waveguide," Opt. Express **21**, 1310–1316 (2013).

[62] E. Izhikevich, *Dynamical systems in neuroscience: the geometry of excitability and bursting* (MIT press, 2006).

[63] T. C. Stewart and C. Eliasmith, "Large-scale synthesis of functional spiking neural circuits," Proceedings of the IEEE **102**, 881–898 (2014).

[64] J. Hoffman and C. Johnson, "A new approach to computational turbulence modeling," Computer Methods in Applied Mechanics and Engineering **195**, 2865 – 2880 (2006).

[65] A. Ammar, B. Mokdad, F. Chinesta, and R. Keunings, "A new family of solvers for some classes of multidimensional partial differential equations encountered in kinetic theory modelling of complex fluids: Part ii: Transient simulation using space-time separated representations," Journal of Non-Newtonian Fluid Mechanics **144**, 98 – 121 (2007).

[66] H. Yoshino and M. Shibata, "Chapter 9 higher-dimensional numerical relativity: Current status," Progress of Theoretical Physics Supplement **189**, 269–309 (2011).

[67] G. Cowan, R. Melville, and Y. Tsividis, "A vlsi analog computer/digital computer accelerator," Solid-State Circuits, IEEE Journal of **41**, 42–53 (2006).

[68] N. Ratier, "Analog computing of partial differential equations," in "Sciences of Electronics, Technologies of Information and Telecommunications (SETIT), 2012 6th International Conference on," (2012), pp. 275–282.

[69] K. E. Friedl, A. R. Voelker, A. Peer, and C. Eliasmith, "Human-inspired neurorobotic system for classifying surface textures by touch," IEEE Robotics and Automation Letters **1**, 516–523 (2016).

[70] A. Mundy, J. Knight, T. Stewart, and S. Furber, "An efficient spinnaker implementation of the neural engineering framework," in "Neural Networks (IJCNN), 2015 International Joint Conference on," (2015), pp. 1–8.

[71] A. Diamond, T. Nowotny, and M. Schmuker, "Comparing neuromorphic solutions in action: implementing a bio-inspired solution to a benchmark classification task on three parallel-computing platforms," Frontiers in Neuroscience **9** (2016).

[72] T. C. Stewart, T. DeWolf, A. Kleinhans, and C. Eliasmith, "Closed-loop neuromorphic benchmarks," Frontiers in Neuroscience **9** (2015).

[73] G. T. Reed, G. Mashanovich, F. Y. Gardes, and D. J. Thomson, "Silicon optical modulators," Nat Photon **4**, 518–526 (2010).

[74] D. Patel, S. Ghosh, M. Chagnon, A. Samani, V. Veerasubramanian, M. Osman, and D. V. Plant, "Design, analysis, and transmission system performance of a 41 ghz silicon photonic modulator," Optics express **23**, 14263—14287 (2015).

[75] Intel Corporation, *Intel 64 and IA-32 Architectures Optimization Reference Manual* (2016).